



Hydrothermal synthesis of novel heterostructured $\text{Fe}_2\text{O}_3/\text{Bi}_2\text{S}_3$ nanorods with enhanced photocatalytic activity under visible light

Ahmed Helal^a, Farid A. Harraz^{a,b,*}, Adel A. Ismail^{a,*}, Tarek M. Sami^c, I.A. Ibrahim^a

^a Nanostructured Materials and Nanotechnology Division, Central Metallurgical Research and Development Institute (CMRDI), P.O. 87 Helwan, Cairo 11421, Egypt

^b Promising Centre for Sensors and Electronic Devices (PCSED), Advanced Materials and Nano-Research Centre, Najran University, P.O. Box: 1988, Najran 11001, Saudi Arabia

^c Tabbin Institute for Metallurgical Studies, (TIMS), P.O.109 Helwan Cairo 11421, Egypt

ARTICLE INFO

Article history:

Received 3 January 2017

Received in revised form 13 April 2017

Accepted 2 May 2017

Available online 3 May 2017

Keywords:

$\text{Fe}_2\text{O}_3/\text{Bi}_2\text{S}_3$ nanorods

Hydrothermal

Photocatalyst

Methylene blue

Phenol

ABSTRACT

The development of efficient visible-light photocatalyst heterostructures remains a major concern for obtaining desirable material properties and effective carrier transformation. Here, we demonstrate, for the first time, the synthesis of novel heterostructures of $\text{Fe}_2\text{O}_3/\text{Bi}_2\text{S}_3$ nanorods via a one-step hydrothermal route and employed effectively as visible-light-driven photocatalysts for the degradation of organic pollutants of methylene blue dye (MB) and phenol. TEM and FE-SEM images displayed that $\text{Fe}_2\text{O}_3/\text{Bi}_2\text{S}_3$ heterostructure is nanorods with ~ 30 – 60 nm diameter and 0.5 – 1 μm length. The newly prepared $\text{Fe}_2\text{O}_3/\text{Bi}_2\text{S}_3$ nanorods exhibit greatly enhanced photocatalytic activity toward both MB and phenol compared to pure Bi_2S_3 and the heterostructure with low molar ratio of 0.06 $\text{Fe}_2\text{O}_3/\text{Bi}_2\text{S}_3$ exhibits the best photocatalytic activity under visible light irradiation. A maximum degradation efficiency of MB and phenol $\sim 90\%$ and 96% was accomplished using $\text{Fe}_2\text{O}_3/\text{Bi}_2\text{S}_3$ nanorods compared to only 60% and 69% using pure Bi_2S_3 , respectively. The photodegradation rates for MB and phenol are promoted respectively as ~ 2.6 and 3 times using $\text{Fe}_2\text{O}_3/\text{Bi}_2\text{S}_3$ heterostructure higher than pure Bi_2S_3 . Photoluminescence spectra measurement along with the calculation of relative band alignment indicated that $\text{Fe}_2\text{O}_3/\text{Bi}_2\text{S}_3$ heterostructure significantly suppress the recombination of photogenerated charge carriers, which is beneficial to improve the photocatalytic activity. The facile synthesis approach, unique photocatalytic activity and excellent reusability of the current Fe_2O_3 modified Bi_2S_3 nanostructure make it a promising photocatalyst for the environmental remediation related fields.

© 2017 Elsevier B.V. All rights reserved.

1. Introduction

Water pollution is a dominant component of environmental concerns and remains a major problem to be solved for a better quality of life. Contaminated wastewater is widely generated as effluents from different industries including petrochemical, textile, pharmaceutical and others [1]. Phenol is classified among the most toxic compounds and can present at considerable concentration in some industrial effluents [2]. In general, the concentration of phenol may vary from a few ppm up to 4 g/L, in a severe pollution case [3], whereas according to the Environmental Protection

Agency (EPA) regulations, the maximum allowed level of phenol is 5 ppm (19 mg/ m^3) [4]. Even at very low concentration, phenol can be a very harmful to living organisms. For example, ingestion of phenol-contaminated water in human body may cause protein degeneration, erosion of tissues, damages to the kidneys, liver, etc., [5]. Another type of organics includes synthetic dyes which are often found in the environment as a result of their wide industrial uses such as in cosmetics, colored paper, textiles, inks, plastics and food. More than $100,000$ different commercial dyes and pigments are available with ~ 7 – 10 tons of dyestuff produced annually [6,7]. The discharge of very low level concentration of dyes (~ 1 ppm for some dyes) would have hazardous effects on environment as well as the biological life [2]. Wastewater is one of the main sources that releasing ~ 10 – 15% of the overall dye production into the environment [8]. The natural decomposition of some dyes could lead to the formation of carcinogenic compounds [9,10]. Therefore, there has been increasing interest to harness and develop the advanced oxidation processes (AOPs) as efficient, advantageous approach for

* Corresponding authors at: Nanostructured Materials and Nanotechnology Division, Central Metallurgical Research and Development Institute (CMRDI), P.O. 87 Helwan, Cairo 11421, Egypt.

E-mail addresses: fharraz68@yahoo.com, faharraz@nu.edu.sa (F.A. Harraz), adelali141@yahoo.com (A.A. Ismail).

the degradation of organic species in wastewater. Among the AOPs, photocatalysis under visible or ultraviolet (UV) light is a key strategy for water decontamination as it can lead to fast, complete mineralization of pollutants with no harmful residues and has been extensively studied as a technology of choice in this field [11–13].

The design of new heterostructured semiconductors using a simple, efficient technique is an existing challenge in materials science and chemical engineering fields [14]. The fabrication of appropriate heterostructure would provide better band gaps alignment which could lead to an effective separation of the photogenerated charge carriers [15]. Good overlapping between the electronic states of the heterostructure interface likely promotes intra-particle charge transfer [16,17]. Unique category of heterostructures is the plasmonic nanoparticles coupled with different semiconductors including for examples Au-supported CdS catalysts and Au/TiO₂ nanohybrids for the photocatalytic hydrogen production [18,19], AgNPs/black phosphorus nanosheets for visible-light photocatalysis [20] and AuNPs with CH₃NH₃PbI₃ perovskite structures [21]. Such unique material characteristics make it possible for the harvesting of solar light, and hence their potential uses in photocatalysis, optoelectronics, photovoltaics, and others [22]. Binary metal chalcogenides with a formula A₂^VB₃^{VI} (A = As, Sb, Bi; B = S, Se, Te) are categorized as one of the leading, attractive class of materials [23]. Particularly, bismuth sulphide (Bi₂S₃) is well studied for its potential applications in photo-electrochemical solar cells [24,25], lithium ion batteries [26], gas sensors [27], Schottky diodes [28], thermoelectricity [29], and hydrogen storage [30]. Bi₂S₃ has a direct narrow band gap (1.3–1.7 eV) [31], which could absorb visible light ($\lambda \leq 800$ nm), allowing its proper use as a visible-light photocatalyst [32]. However, due to its narrow band gap, a rapid recombination of the photogenerated charge carriers is often observed, which limits greatly the photocatalytic activity under either UV or visible light irradiation [14]. On the other hand, transition metal oxides have special interest in developing cost-effective, alternative photocatalysts to the conventionally employed noble metal-based catalysts [33]. Among these, Fe₂O₃ has been explored as low-cost, environmental friendliness catalysts for a range of catalytic processes including oxidations [34], couplings [35], and alkylation-based processes [36]. Having a band gap of ca. 2.2 eV, Fe₂O₃ could act also as a visible-light-driven photocatalyst [37]. Nevertheless, the photocatalytic activity of pure Fe₂O₃ is not satisfactory owing to its low carrier mobility, short life of minority carriers (~10 ps) and diffusion length (~2–4 nm) [38]. Aiming to overcome these limitations, we present a simple hydrothermal route for synthesizing hetero-nanostructure of Fe₂O₃/Bi₂S₃ nanorods, which, to the best of our knowledge, has not been developed so far. The as-obtained Fe₂O₃ modified Bi₂S₃ nanorods exhibited enhanced photocatalytic activities for degrading both methylene blue (MB) dye and phenol as a two models of organic pollutants under visible light irradiation. The synthesis and characterization of Fe₂O₃/Bi₂S₃ photocatalyst, mechanism of catalytic performance along with its reusability have been addressed and thoroughly discussed.

2. Experimental

2.1. Material

All chemicals used in this study were analytical grade reagents and were purchased from Sigma-Aldrich. Bismuth (III) nitrate penta-hydrate Bi(NO₃)₃·5H₂O and thiourea (NH₂)₂S were employed as precursors of Bi and S, respectively. Iron nitrate Fe(NO₃)₃·9H₂O was chosen as a precursor for Fe₂O₃. Methylene blue (MB) dye and phenol were used as target organic molecules.

2.2. Hydrothermal synthesis of Fe₂O₃/Bi₂S₃ nanostructures

Fe₂O₃ modified Bi₂S₃ nanorods were synthesized by a one-step hydrothermal process, adapted from our recently reported method for obtaining pure Bi₂S₃ [39]. In a typical synthesis protocol, 4.0 g Bi(NO₃)₃·5H₂O and 1.25 g (NH₂)₂S were first dissolved in 100 mL deionized water. Then, different amounts of Fe(NO₃)₃·9H₂O ~0.04, 0.08, 0.12, 0.16, 0.20, 0.24 and 0.28 g were added to the above solution under vigorous stirring for 10 min at 60 °C to obtain 0.01, 0.02, 0.03, 0.04, 0.05, 0.06, and 0.07 Fe₂O₃:Bi₂S₃ molar ratios, respectively. The solution was transferred into a Teflon-lined stainless steel autoclave and heated at 180 °C for 20 h. After the autoclave was cooled to room temperature, the resulting product was separated by centrifugation and washed several times with water and absolute ethanol and finally dried at 60 °C for 8 h.

2.3. Characterization of photocatalysts

The phase and crystal structure of the as-synthesized photocatalysts were examined by X-ray diffraction (XRD) using a BRUKER D8 advance with Cu target (λ 1.54 Å). Measurements were collected at 40 kV and 40 mA, for 2 θ from 10 to 80°, with a 0.05° step size and 3 s count time. For morphological investigation, a JEOL JSM-2010 transmission electron microscope (TEM) operating at 200 kV was used with recording selected-area electron diffraction (SAED) pattern. A trace amount of powder was dispersed in ethanol followed by 20 min ultrasonication. A carbon film coated copper grid was immersed into the dispersion and left for drying. FESEM (QUANTA FEG 250) equipped with energy dispersive X-ray spectroscopy (EDS) was also used for further structural and chemical analysis. X-ray photoelectron spectra (XPS) were collected using a VG Escalab 200R electron spectrometer equipped with a MgK α ($h\nu$ = 1253.6 eV, 1 eV = 1.6302 × 10⁻¹⁹ J) X-ray source powered at 100 W. The binding energies (BE) were calibrated reference to the C1 s peak at 284.8 eV. The photoluminescence (PL) spectra were collected at room temperature using F-7000 FL spectrophotometer, HITACHI with a 150 W xenon lamp as an excitation source at 450 nm excitation wavelength. The band gap energy (E_g) of Fe₂O₃/Bi₂S₃ was estimated using diffuse reflectance spectroscopy (DRS). The reflectance spectra in a wavelength range 200–800 nm were measured by a JASCO V-570 UV–vis spectrophotometer equipped with a Labsphere integrating sphere diffuse reflectance accessory using BaSO₄ as a reference [40]. The UV–vis spectra were collected in the diffuse reflectance mode (R) and transformed to the Kubelka-Munk function F(R) to separate the extent of light absorption from scattering. The E_g values were accordingly obtained from the plot of the modified Kubelka-Munk function ($F(R)/E$)² versus the energy of the absorbed light E, according to the following formula [41].

$$F(R)E^2 = \left(\frac{(1-R)^2}{2R} \times h\nu \right)^2$$

2.4. Photocatalytic properties

The photocatalytic activity of heterostructure Fe₂O₃/Bi₂S₃ nanorods was evaluated by the degradation of MB and phenol under visible light irradiation using 1000 W halogen lamp. In a typical process, 0.5 g/L photocatalyst was added to MB [10 mg/L] solution in a quartz photoreactor with water circulation for cooling. Before illumination, the solution was magnetically stirred in the dark for 30 min to reach adsorption equilibrium between the organic pollutants and photocatalysts. Subsequently, the stirred solution was photo-irradiated by visible light. The MB concentration after equilibration was denoted as the initial concentration (C_0). At given time intervals, 3 mL solution was taken and the sus-

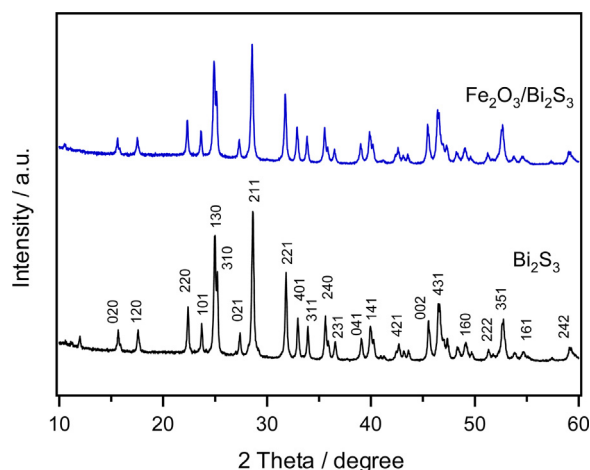


Fig. 1. XRD patterns of hydrothermally synthesized Bi_2S_3 and $\text{Fe}_2\text{O}_3/\text{Bi}_2\text{S}_3$ nanorods.

pendent was removed from the liquid phase by filtration through nylon syringe filters. The filtrates were then analyzed by recording the variation in the UV–vis spectra of MB by using a JASCO V-570 UV–vis spectrophotometer. The photocatalytic activity was calculated using the following formula:

$$\% \text{photocatalytic activity} = (1 - C_t) / C_0 \times 100$$

where C_0 and C_t are the equilibrium concentration of adsorption and the concentration of MB at the irradiation time t , respectively. For photodegradation of phenol, the initial concentration of phenol was 50 mg/L and 2.5 g/L of photocatalysts being added to phenolic solution. The chemical oxygen demand (COD) concentration represents the mineralization extent of organic pollutant in water. Liquors extracted from the solutions at the end of degradation reaction were also used to determine the COD using potassium permanganate standard method.

3. Results and discussions

3.1. Structural investigation and surface analysis

Fig. 1 shows the XRD patterns of the samples obtained as pure Bi_2S_3 and 0.06 $\text{Fe}_2\text{O}_3/\text{Bi}_2\text{S}_3$ nanorods. All the diffraction peaks can be perfectly indexed to an orthorhombic Bi_2S_3 structure (JCPDS Card No. 00-017-0320) with major peaks related to (020), (130), (211), and (221) planes with unit cell constants: $a = 11.15 \text{ \AA}$, $b = 11.30 \text{ \AA}$ and $c = 3.97 \text{ \AA}$ [39]. No other crystalline impurities were observed. For the $\text{Fe}_2\text{O}_3/\text{Bi}_2\text{S}_3$ heterostructure fabricated, only the orthorhombic Bi_2S_3 phase was detected with no phase attributed to the presence of Fe_2O_3 . Absence of Fe_2O_3 is probably due to either a highly dispersed, poor crystalline degree of Fe_2O_3 or its content in the heterostructure is below the XRD limit of detection. Additionally, there is no remarkable shift in the diffraction peak position or peak broadening. However, the intensity of the main diffraction peaks of pure Bi_2S_3 decreased in modified sample of $\text{Fe}_2\text{O}_3/\text{Bi}_2\text{S}_3$, suggesting a possible contribution of Fe_2O_3 in the reorientation of the Bi_2S_3 crystal growth. The existence of Fe_2O_3 was further confirmed by XPS measurement.

Surface composition and chemical states of $\text{Fe}_2\text{O}_3/\text{Bi}_2\text{S}_3$ heterostructure were further analyzed by X-ray photoelectron spectroscopy (XPS). As anticipated, characteristic spectral lines for Fe, O, Bi, C and S are detected in survey XPS spectrum (Fig. 2a). The appearance of C1s peak is likely attributed to adventitious carbon and/or CO_2 adsorbed onto the sample from the atmosphere. As shown in Fig. 2b, the $\text{Bi}4f_{5/2}$ and $\text{Bi}4f_{7/2}$ peaks appear at 164.0 and 158.6 eV, respectively with a typical spin–orbit doublet split-

ting of 5.4 eV, in consistent with the standard Bi^{3+} peaks of Bi_2S_3 [42]. The spectral signals observed between $\text{Bi}4f_{5/2}$ and $\text{Bi}4f_{7/2}$ are related to $\text{S}2p_{1/2}$ at 162.5 eV and $\text{S}2p_{3/2}$ at 161.3 eV. Furthermore, in Fig. 2a, the O1s peak observed at 530.8 eV and the S2s peak detected at 225.5 eV are well-matched respectively with O^{2-} in Fe_2O_3 and S^{2-} in sulphide [43]. Taking into account the atomic sensitivity factors for both Bi and S, the ratio of the area under the peak of $\text{Bi}4f$ to S2s was found stoichiometric with the as-prepared Bi_2S_3 . Fig. 2c exhibits the $\text{Fe}2p$ core-level spectrum with two distinct peaks located at 710.6 eV for $\text{Fe}2p_{3/2}$ and 724.4 eV for the $\text{Fe}2p_{1/2}$, corresponding well with the typical values of the ferric (Fe^{3+}) oxide [44,45]. Obviously, the $\text{Fe}2p_{3/2}$ signal is narrower and stronger with a larger area compared to the $\text{Fe}2p_{1/2}$, which in good agreement with the reported peaks of Fe_2O_3 standard sample [46]. Now, the XPS analysis in combination to the XRD finding confirmed that the main components of as-synthesized heterostructure are Bi_2S_3 and Fe_2O_3 .

The morphology of the product was further examined by SEM and TEM analysis. The FESEM image of $\text{Fe}_2\text{O}_3/\text{Bi}_2\text{S}_3$ heterostructure is shown in Fig. 3a, in which nanorods are formed with a wide size distribution (in diameter and length); the diameter of the small nanorods varied from 30 to 60 nm with an average length of 0.5–1 μm . Bigger nanorods can be detected in the inset image (a) with a diameter of about 500 nm. Aggregation like flower structure composed of a large quantity of tiny nanorods can be also recognized. The EDS recorded as spot analysis revealed that the sample consists mainly of Bi and S elements with stoichiometric ratio of 2:3 matching exactly the value of pure Bi_2S_3 (Fig. 3b). The detailed microstructure was then analyzed using TEM and selected-area electron diffraction (SAED). Fig. 3c illustrates a typical TEM image of the nanorods with $\sim 50 \text{ nm}$ diameter in agreement with the sizes of small nanorods confirmed by SEM. The inset of Fig. 3c describes a magnified section of TEM image c in which small nanoparticles of Fe_2O_3 are attached onto the surface of Bi_2S_3 nanorods. The HRTEM image of a single nanorod (Fig. 3d) shows lattice fringes of 0.56 nm corresponding to the d-spacing of the (200) crystal plane of the orthorhombic Bi_2S_3 [47]. This suggests that the growth of Bi_2S_3 nanorods proceeds along the preferential [001] direction as indicated in our recent work [39]. The bright spots in the SAED pattern (inset of image d) indicate the single-crystallinity of the synthesized Bi_2S_3 . Moreover, the crystalline phase of Fe_2O_3 was further evidenced by HR-TEM image, inset in Fig. 3(d). As revealed, the lattice fringes of $\alpha\text{-Fe}_2\text{O}_3$ are clearly detected, with adjacent lattice planes of 3.7 \AA corresponding to two (012) crystal planes of $\alpha\text{-Fe}_2\text{O}_3$ [48].

The optical behavior of $\text{Fe}_2\text{O}_3/\text{Bi}_2\text{S}_3$ heterostructure was further investigated by UV–vis diffuse reflectance spectroscopy (DRS). As shown in Fig. 4, a broad absorption spectrum was detected which essentially indicates a visible-light activity of the $\text{Fe}_2\text{O}_3/\text{Bi}_2\text{S}_3$ heterostructure. The band gap (E_g) was calculated from the plot of the modified Kubelka–Munk function $[F(R)E^2]$ versus the energy of the absorbed light E [41] as described in the inset of Fig. 4, and was found to be 2.13 eV. This E_g value is a bit higher than the value estimated for the hydrothermally grown phase of Bi_2S_3 nanorods (1.45 eV) that recently reported by our group [39], as well as the average reported range of (1.3–1.7 eV) [31]. However, the key optical feature here is that the synthesized $\text{Fe}_2\text{O}_3/\text{Bi}_2\text{S}_3$ heterostructure with a modified band gap is still expected to show visible-light driven photocatalytic activity.

3.2. Photocatalytic activity

The photocatalytic activity of the as-obtained $\text{Fe}_2\text{O}_3/\text{Bi}_2\text{S}_3$ heterostructure at different Fe_2O_3 contents was evaluated by the visible-light photodegradation of two model pollutants: MB dye

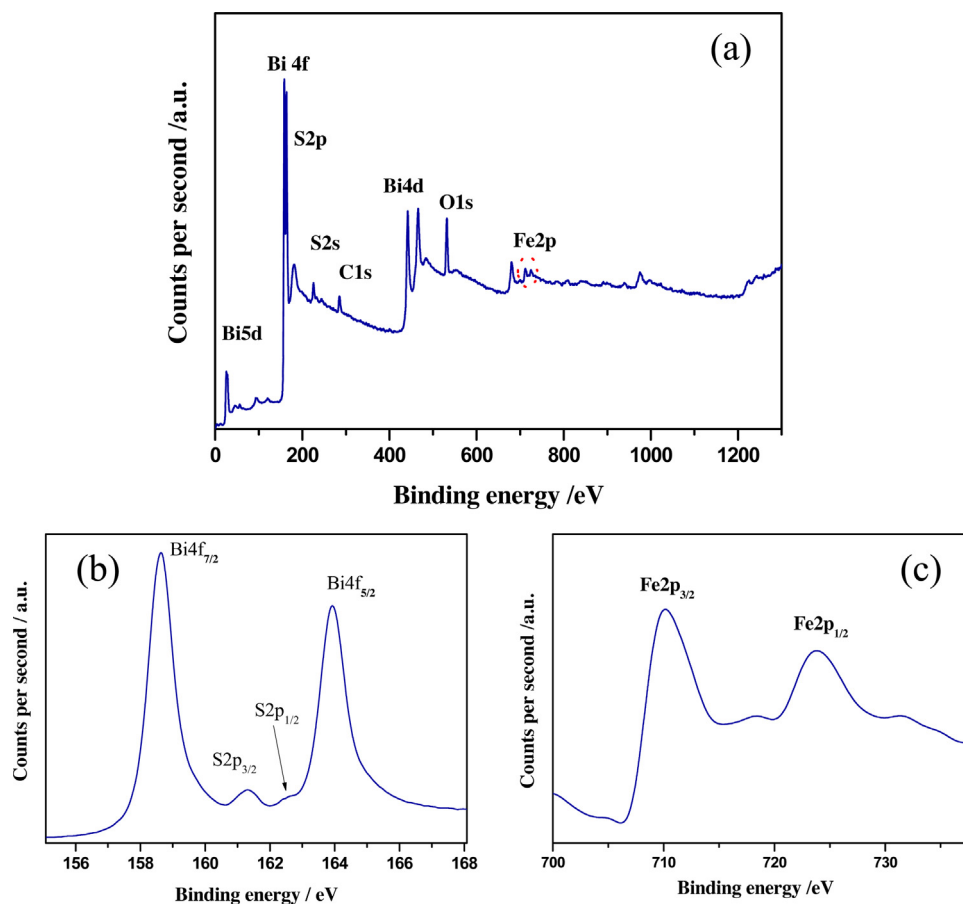


Fig. 2. (a) Survey XPS spectrum of $\text{Fe}_2\text{O}_3/\text{Bi}_2\text{S}_3$ nanorods; (b) High-resolution Bi 4f XPS spectrum and (c) High-resolution Fe 2p XPS spectrum.

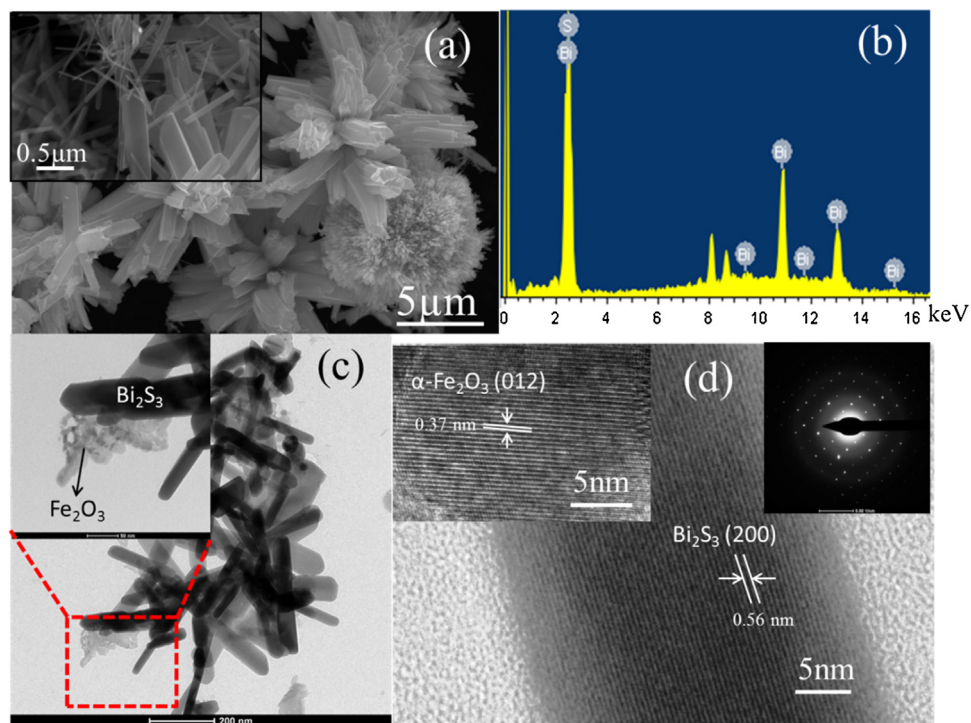


Fig. 3. (a) FESEM image of $\text{Fe}_2\text{O}_3/\text{Bi}_2\text{S}_3$ heterostructure with a magnified image in the inset; (b) The corresponding EDS chemical analysis; (c) TEM image of a typical heterostructure with a magnified section in the inset and (d) HR-TEM image taken at one nanorod (inset shows the SAED patterns) with a HR-TEM image of $\alpha\text{-Fe}_2\text{O}_3$.

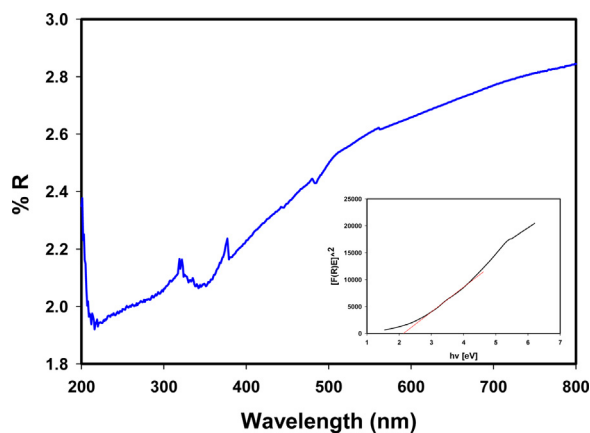


Fig. 4. UV-vis diffuse reflectance spectra of $\text{Fe}_2\text{O}_3/\text{Bi}_2\text{S}_3$ heterostructure. Inset shows the plot of transferred Kubelka–Munk vs. energy of the light absorbed.

and phenol as a colorless organic molecule. Firstly, the adsorption capability and visible light photodegradation rate of MB using pure Bi_2S_3 and $\text{Fe}_2\text{O}_3/\text{Bi}_2\text{S}_3$ heterostructure prepared with different concentrations of Fe_2O_3 were examined as shown in Fig. 5a. As revealed, the adsorption capacity for all tested samples is quite similar and found to be below the 10%. For the heterostructure with 0.06 $\text{Fe}_2\text{O}_3/\text{Bi}_2\text{S}_3$ molar ratio, best photocatalytic degradation of ~90% of MB was obtained after 300 min. Typical absorbance versus wavelength as a function of irradiation time during the photodegradation of MB using both pure Bi_2S_3 phase and $\text{Fe}_2\text{O}_3/\text{Bi}_2\text{S}_3$ heterostructure is depicted respectively in Fig. 5b and c, with a comparative photocatalytic activity presented in Fig. 5d. As depicted in Fig. 5b and c, the absorption peaks of MB located at 292 and 664 nm quenched gradually with irradiation time with MB color

change, indicating a decomposition of the dye chromophoric structure. A maximum degradation efficiency of ~90% was achieved after 300 min using 0.06 $\text{Fe}_2\text{O}_3/\text{Bi}_2\text{S}_3$ molar ratio compared to only 60% using pure phase of Bi_2S_3 under identical experimental conditions, Fig. 5d, indicating a significant enhancement in the photocatalytic activity after the addition of Fe_2O_3 into Bi_2S_3 . Additionally, the blank experiments conducted under visible-light irradiation in absence of catalyst indicated that the photolysis degree of the dye was negligible, Fig. 5d. It has long been known that the MB de-colorization could be achieved via an oxidative degradation or by a two-electron reduction approach [49]. The band absorption often appears at 256 nm corresponding to the leuco-MB was not detected, confirming that the MB de-colorization is presumably due to the oxidative degradation.

Similarly, the results of photodegradation of phenol under visible-light irradiation are shown in Fig. 6. The comparative experiments shown in Fig. 6a indicated a remarkable enhancement of photocatalytic activity for degrading colorless phenol using $\text{Fe}_2\text{O}_3/\text{Bi}_2\text{S}_3$ heterostructure compared to pure Bi_2S_3 . Specifically, the absorption peaks of phenol locating at 234.5 and 287.5 nm [50] decreases with irradiation time (Fig. 6b), reaching a maximum degradation value of 96% after 300 min irradiation compared to only 69% obtained using pure Bi_2S_3 (Fig. 6c). In agreement with the result of MB photodegradation, the presence of Fe_2O_3 in the final photocatalyst product induced obvious enhancement in the photocatalytic activity toward phenol. The photocatalytic reaction rates for each individual process were also calculated. The photocatalytic reaction of MB and phenol follows first-order kinetics expressed by: $\ln(C_0/C) = kt$, in which C_0 is the concentration of target molecule at the adsorption equilibrium and C is the residual concentration after irradiation time intervals t and k represents the apparent rate constant. The plots of $\ln(C_0/C)$ versus t are linear (Fig. 7a and b), indicating that the photodegradation of both MB and phenol on the

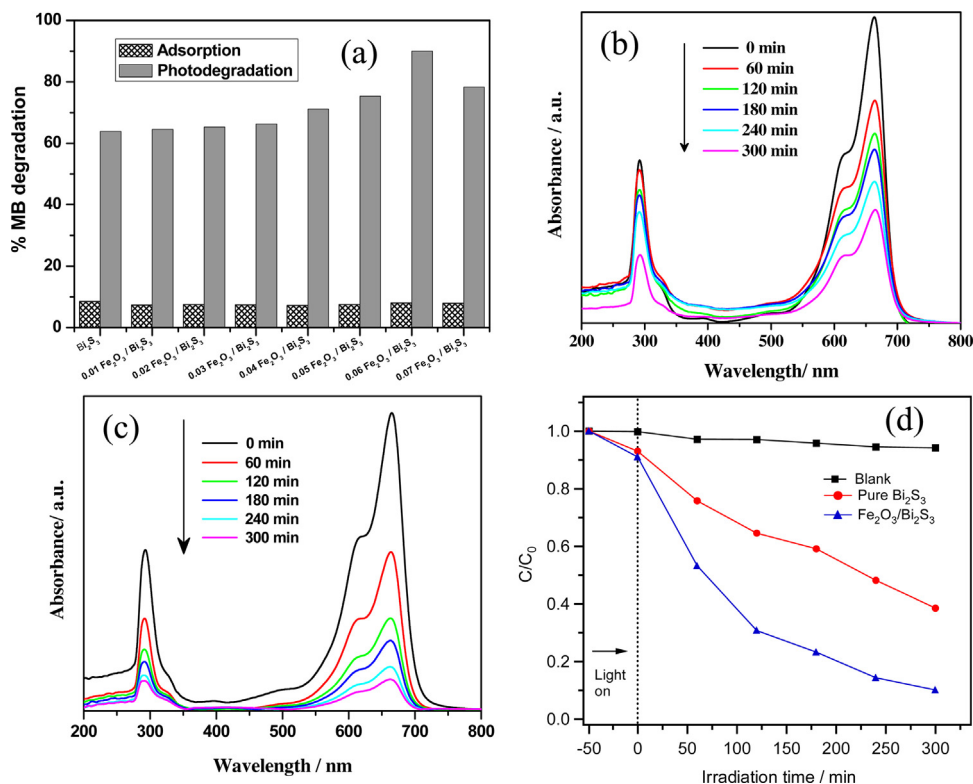


Fig. 5. (a) Adsorption and visible light photodegradation rate of MB using pure Bi_2S_3 and $\text{Fe}_2\text{O}_3/\text{Bi}_2\text{S}_3$ heterostructure with different concentrations of Fe_2O_3 . Absorbance vs. wavelength as a function of irradiation time for the photodegradation of MB on: (b) pure Bi_2S_3 and (c) $\text{Fe}_2\text{O}_3/\text{Bi}_2\text{S}_3$ heterostructure. (d) A comparative photocatalytic activities of pure Bi_2S_3 and $\text{Fe}_2\text{O}_3/\text{Bi}_2\text{S}_3$ heterostructure. MB concentration: 10 mg/L; volume of MB: 200 mL; photocatalyst loading: 100 mg.

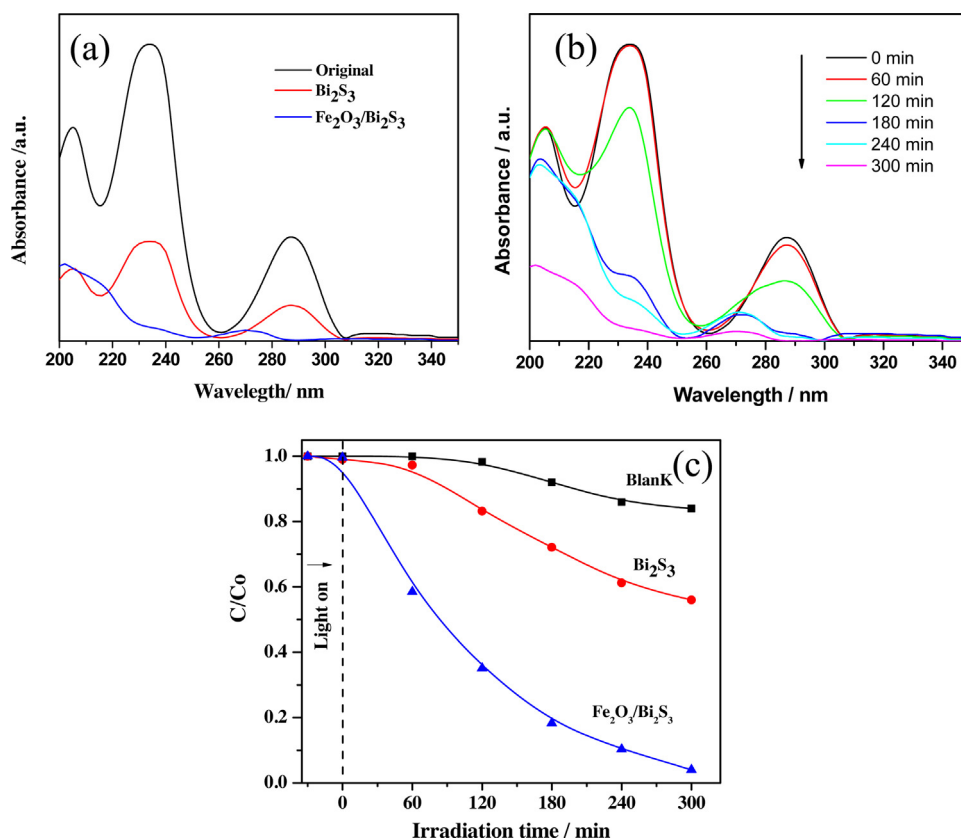


Fig. 6. (a) Absorbance vs. wavelength under optimum condition for the photodegradation of phenol on pure Bi_2S_3 and $\text{Fe}_2\text{O}_3/\text{Bi}_2\text{S}_3$ heterostructure under visible light irradiation. (b) Absorbance vs. wavelength as a function of irradiation time for the photodegradation of phenol on $\text{Fe}_2\text{O}_3/\text{Bi}_2\text{S}_3$ heterostructure. (c) A comparative photocatalytic activities of pure Bi_2S_3 and $\text{Fe}_2\text{O}_3/\text{Bi}_2\text{S}_3$ heterostructure toward phenol. Phenol concentration: 50 mg/L; volume of phenol: 200 mL; photocatalyst loading: 500 mg.

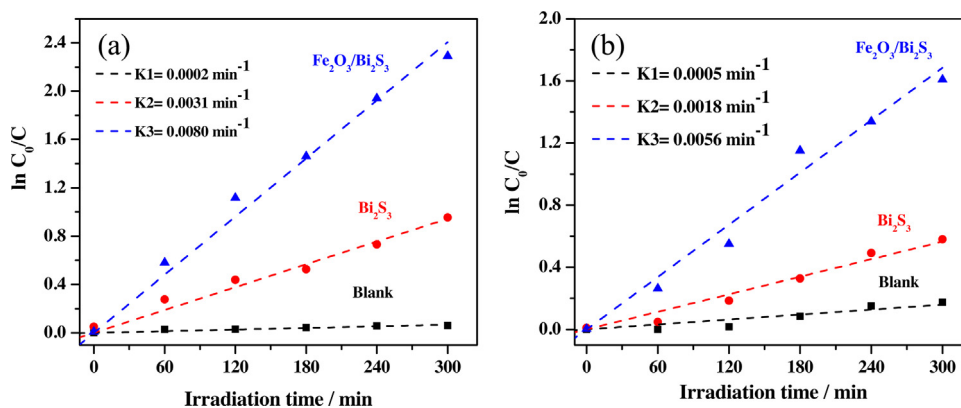


Fig. 7. Plots of $\ln(C_0/C)$ versus irradiation time for blank, pure Bi_2S_3 and $\text{Fe}_2\text{O}_3/\text{Bi}_2\text{S}_3$ heterostructure photocatalysts measured under visible light irradiation for (a) MB and (b) phenol.

current photocatalysts obeys the first-order reaction kinetics. The fitting parameters and calculations again showed that the reaction rate was fastest for the $\text{Fe}_2\text{O}_3/\text{Bi}_2\text{S}_3$ heterostructure. The k values obtained for MB are respectively 0.0031 and 0.0080 min^{-1} for pure Bi_2S_3 and $\text{Fe}_2\text{O}_3/\text{Bi}_2\text{S}_3$ heterostructure (2.6 times larger), while the values of phenol were respectively 0.0018 and 0.0056 min^{-1} (3 times larger).

The mineralization of both MB and phenol was evaluated by measuring the chemical oxygen demand (COD). The mineralization degree of MB and phenol is showed in Fig. 8a and b, respectively. In both cases, it is revealed that the mineralization was significantly enhanced upon using $\text{Fe}_2\text{O}_3/\text{Bi}_2\text{S}_3$ heterostructure compared to Bi_2S_3 alone. In MB model (Fig. 8a), the COD value was found to

reduce in the presence of $\text{Fe}_2\text{O}_3/\text{Bi}_2\text{S}_3$ nanorods from 20 ppm to 10 ppm after 300 min irradiation compared to a remaining 17 ppm using pure Bi_2S_3 . In case of phenol, Fig. 8b, the COD reduced in the presence of $\text{Fe}_2\text{O}_3/\text{Bi}_2\text{S}_3$ nanorods from 61 ppm to 4 ppm compared to a remaining value of 30 ppm using pure Bi_2S_3 under the same experimental conditions. The results of COD analysis confirmed the enhanced photocatalytic behavior of $\text{Fe}_2\text{O}_3/\text{Bi}_2\text{S}_3$ nanorods towards both MB and phenol, in a similar way as obtained using the UV–vis spectroscopy measurement. However, the degradation efficiencies evaluated using both analytical techniques are more comparable to each other in case of phenol than the MB.

Reactive species trapping experiments were further conducted to effectively detect the induced species during the photocatalytic

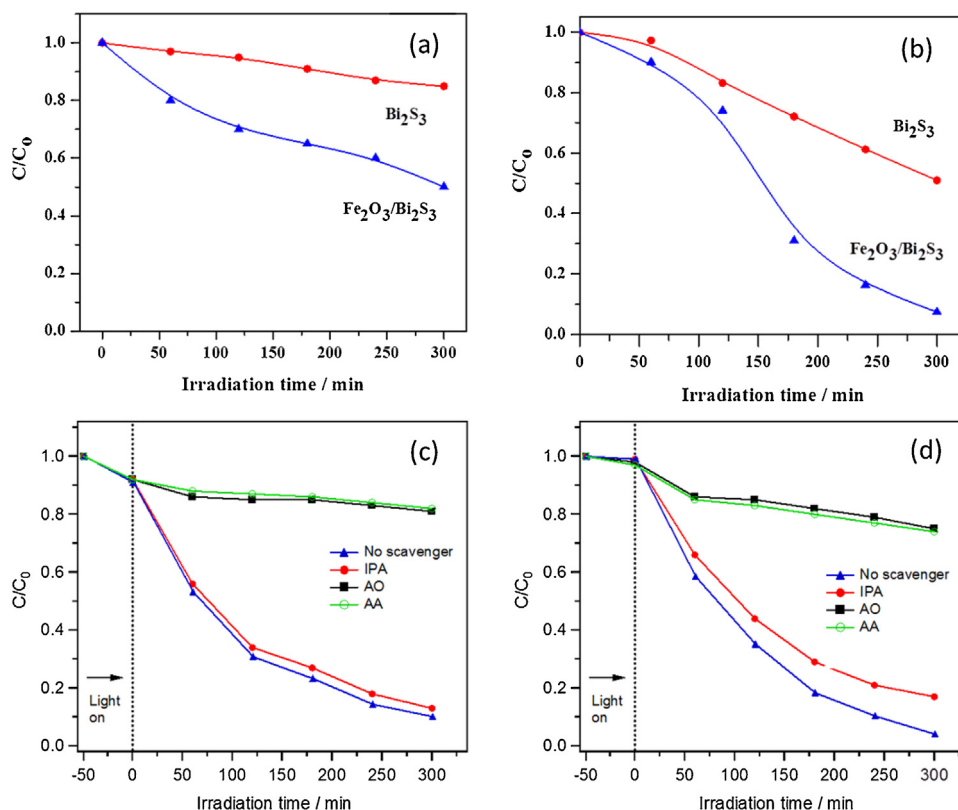


Fig. 8. Extent of mineralization by COD using pure Bi₂S₃ and Fe₂O₃/Bi₂S₃ heterostructure under visible light irradiation towards (a) MB and (b) phenol. Reactive species trapping experiments during the photodegradation of MB (a) and phenol (b) under visible light irradiation using Fe₂O₃/Bi₂S₃ photocatalyst.

event. In this work, ammonium oxalate (AO, 0.01 M), ascorbic acid (AA, 0.01 M) and isopropyl alcohol (IPA, 0.01 M) were used as scavengers for the photogenerated holes (h^+), superoxide anion radicals ($\bullet O_2^-$) and hydroxyl radicals ($\bullet OH$), respectively [51,52]. According to the results shown in Fig. 8(c) and (d), the photocatalytic degradation of MB and phenol is notably suppressed in the presence of AO and AA, indicating that both h^+ and $\bullet O_2^-$ are the dominant active species in the photocatalytic process. In contrast, with the addition of IPA, the trapping reagent for $\bullet OH$, sluggish decrease in the photocatalytic activity is observed, implying that $\bullet OH$ would not significantly take part as a photo-oxidant to either MB or phenol photodegradation.

The present heterostructure based photocatalysts could be recycled and reused five times without significant loss of degradation efficiency towards both MB and phenol, which is a key issue for a possible practical application. In case of MB, the photocatalytic degradation efficiency was 90% in the first cyclic run, dropped to 77% in cycle five (Fig. 9a). The reusability tests in case of phenol are shown in Fig. 9b, which revealed that the degradation degree decreased from 96% to 88% after 5 cyclic runs. The deactivation of the Fe₂O₃/Bi₂S₃ photocatalyst is probably related to the leaching of active species or weight loss during the repeated filtration process to separate the catalyst from reaction medium.

3.3. The role of Fe₂O₃ and photocatalytic mechanism

Generally, the photocatalytic activity of hybrid photocatalysts in decontaminating organic pollutants has long been known to be closely affected by the adsorption affinity of the catalyst, better utilization of light, effective separation of photogenerated carriers and surface catalytic response [53–57]. Firstly, as described in Fig. 4, the addition of Fe₂O₃ into Bi₂S₃ does not notably increase the adsorption capability of the heterostructure. Secondly, the

modification of band gap energy after introduction of Fe₂O₃ does not imply a better utilization of solar light compared to pristine Bi₂S₃. Additionally, previous reports have shown that pure Fe₂O₃ nanostructures exhibited negligible visible-light photocatalytic performance towards the degradation of phenol or dyes [58,59]. Thus, in order to clarify the catalytic role of Fe₂O₃ in current modified heterostructure and understand the charge transfer mechanism, we have employed two independent approaches; (i) calculation of relative band energy positions to properly evaluate the possibility of band coupling between Fe₂O₃ and Bi₂S₃ to form an efficient heterostructure and (ii) measurement of photoluminescence (PL) spectra which is considered as a useful technique to investigate the separation efficiency of the photogenerated carriers in semiconductors.

The energy level and band structure of Fe₂O₃ and Bi₂S₃ can be calculated according to the following empirical Formulae (1) and (2) [60,61]:

$$E_{CB} = X - 0.5E_g + E_0 \quad (1)$$

$$E_{VB} = E_g + E_{CB} \quad (2)$$

where E_{CB} and E_{VB} represent respectively the conduction and valence band edge, E_g is the band gap energy, X is the absolute electronegativity of the semiconductor and E_0 is a measuring scale factor for the redox level of the reference electrode with respect to the absolute vacuum scale; $E_0 = -4.5$ eV for (NHE) normal hydrogen electrode. The reported values of X for Fe₂O₃ and Bi₂S₃ are respectively 5.88 and 5.28 eV [62,63]. Using the above formulae and considering the typical E_g value of Fe₂O₃ as 2.2 eV and for Bi₂S₃ as 1.45 eV [62,39], the E_{CB} and E_{VB} levels of Fe₂O₃ could be estimated as 0.28 and 2.48 eV versus NHE, respectively. Similarly, the E_{CB} and E_{VB} values of Bi₂S₃ equal to 0.06 and 1.48 eV versus NHE, respectively. As revealed, both E_{CB} and E_{VB} of Fe₂O₃ are more posi-

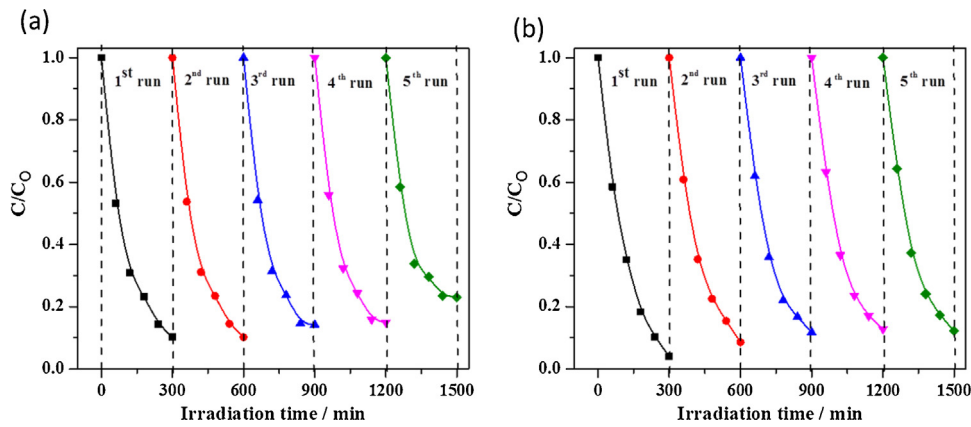


Fig. 9. The stability of $\text{Fe}_2\text{O}_3/\text{Bi}_2\text{S}_3$ heterostructure after 5 cycles of photocatalytic degradation under visible light irradiation for (a) MB and (b) phenol.

tive than the corresponding values of Bi_2S_3 , and hence a separation and efficient charge transfer become thermodynamically favorable. Fig. 10a shows a schematic representation of the band energy levels of Fe_2O_3 and Bi_2S_3 with the possible charge separation process. The illustration in Fig. 10a could explain the enhanced photocatalytic activity of the heterostructure owing to efficient carrier separation and improved charge transfer process. To further support the above finding of good coupling of band energy levels, room temperature PL emission spectra (excited at 400 nm) of pure Bi_2S_3 and $\text{Fe}_2\text{O}_3/\text{Bi}_2\text{S}_3$ nanorods are displayed in Fig. 10b. It is commonly agreed that a lower PL emission spectra is a direct indication of a lower recombination rate of photogenerated $e^- - h^+$ pairs [64]. As revealed, the spectral PL intensity of $\text{Fe}_2\text{O}_3/\text{Bi}_2\text{S}_3$ heterostructure is partially quenched compared to the spectrum obtained for pure Bi_2S_3 phase. This suggests again a better and efficient separation of the photogenerated electrons and holes.

To further understand the catalytic mechanism, Fig. 10a reveals that under irradiation, Fe_2O_3 and Bi_2S_3 could be photoexcited generating holes (h^+) and electrons (e^-). The photoinduced (h^+) in E_{VB} of Fe_2O_3 migrate to Bi_2S_3 because the VB of Bi_2S_3 locates at a less positive potential than that of Fe_2O_3 and simultaneously the photoinduced (e^-) in Bi_2S_3 are injected to the E_{CB} of Fe_2O_3 owing to its more positive position compared to the CB level of Bi_2S_3 . Such an energetic situation of the heterostructure would make it possible that the photogenerated (e^-) and (h^+) are efficiently separated and thus the target pollutant will be readily photodegraded to the final products. Considering that the typical redox potential of (O_2/OH^-) equals 0.401 eV, the (e^-) at the CB of Fe_2O_3 ($E_{\text{CB}} = 0.28$ eV) could be involved in the reduction of O_2 to OH^- . Contrary, the photoinduced (h^+) at the VB of Bi_2S_3 ($E_{\text{VB}} = 1.48$ eV) which is less positive than the standard reduction potential of ($\text{OH}^-/\bullet\text{OH}$) = 1.99 eV [65] will not be able to oxidize OH^- to $\bullet\text{OH}$. This implies that the photoinduced (h^+) play more decisive role in the photocatalytic event than the $\bullet\text{OH}$. This means, the $\bullet\text{OH}$ is not expected to be a dominant photo-oxidant, while direct transfer of (h^+) and $\bullet\text{O}_2^-$ would preferably take part in the photocatalytic process over the surface of $\text{Fe}_2\text{O}_3/\text{Bi}_2\text{S}_3$ heterostructure. Indeed, such a conclusion from the relative energy band positions and the standard redox potentials is consistent with the above active species trapping results. Now, the most favorable reaction steps taking part in the current photocatalytic event can be accordingly summarized as follows:

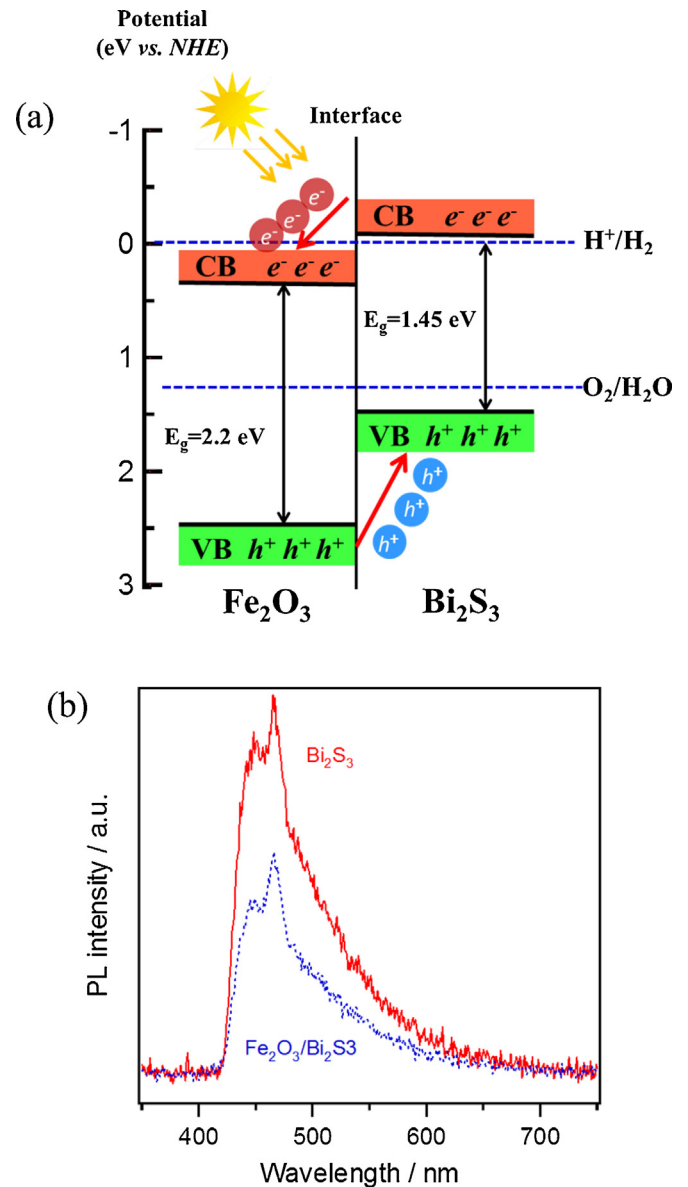
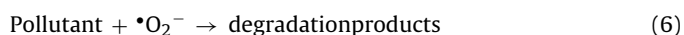
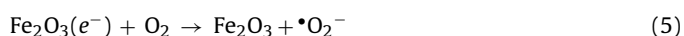
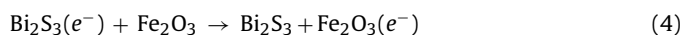


Fig. 10. (a) Deduced energy band levels of $\text{Fe}_2\text{O}_3/\text{Bi}_2\text{S}_3$ heterostructure showing the charge separation process. (b) Room temperature PL spectra of Bi_2S_3 and $\text{Fe}_2\text{O}_3/\text{Bi}_2\text{S}_3$ excited at $\lambda = 400$ nm.



4. Conclusions

In summary, novel visible-light photocatalyst heterostructures composed of Bi_2S_3 nanorods with low contents of Fe_2O_3 have been synthesized by a simple one-step hydrothermal procedure. The addition of Fe_2O_3 into the Bi_2S_3 nanorods was found to enhance its photocatalytic activity. The photodegradation rates of $\text{Fe}_2\text{O}_3/\text{Bi}_2\text{S}_3$ nanorods are greater 2.6 and 3 times than pure Bi_2S_3 for the degradation of MB and phenol, respectively. The current developed photocatalysts showed excellent stability and reusability as evidenced by the successive cyclic runs for 5 times for both MB and phenol. As revealed from the photoluminescence spectra and the relative band position of the heterostructure, the enhanced photocatalytic performance is essentially related to the efficient separation of photogenerated carriers. Moreover, the low content of Fe_2O_3 could play an efficient catalytic role and hence is considered as an alternative to noble metals, which is advantageous from the economic point of view. The research findings reported here are promising to enable further understanding of the concept of design and fabrication of other hetero-nano-structures for obtaining efficient visible-light photocatalysts for environmental applications.

References

- [1] F. Belab, A.H. Meniai, M.B. Lehocine, Elimination of phenol by adsorption onto mineral/polyaniline composite solid support, *Energy Procedia* 18 (2012) 1254–1260.
- [2] H. Ghodbane, O. Hamdaoui, Intensification of sonochemical decolorization of anthraquinonic dye Acid Blue 25 using carbon tetrachloride, *J. Ultrason. Sonochem.* 16 (2009) 455–461.
- [3] R.G. Bond, C.P. Straub, *Handbook of Environmental Control*, vol. IV, CRC Press, USA, 1974.
- [4] E.L. Barker, E.B. Peter, H.F. Petrecia, S.K. Grant, Phenol poisoning due to contaminated drinking water, *Arch. Environ. Health* 33 (2) (1978) 89–94.
- [5] R. Quadeer, A.H. Rehan, A study of the adsorption of phenol by activated carbon from aqueous solutions, *J. Chem.* 26 (2002) 357–361.
- [6] G. McMullan, C. Meehan, A. Conneely, N. Kirby, T. Robinson, P. Nigam, I.M. Banat, R. Marchant, W.F. Smyth, Microbial decolorization and degradation of textile dyes: mini review, *Appl. Microbiol. Biotechnol.* 56 (2001) 81–87.
- [7] C.I. Pearce, J.R. Lloyd, J.T. Guthrie, The removal of color from textile wastewater using whole bacterial cells: a review, *J. Dyes Pigments* 58 (2003) 179–196.
- [8] H. Zollinger, *Color Chemistry, Synthesis Properties and Application of Organic Dyes and Pigments*, VCH Publishers, New York, 2004.
- [9] S. Parsons, *Advanced Oxidation Processes for Water and Wastewater*, IWA Publishing, London, UK, 2004.
- [10] M.Z. Alam, S. Ahmad, A. Malik, M. Ahmad, Study on Mutagenicity and genotoxicity of tannery effluents used for irrigation purpose at Kanpur, *J. Ecotoxicol. Environ. Saf.* 73 (2010) 1620–1628.
- [11] A.B. Prevot, A. Basso, C. Baiocchi, M. Pazzi, G. Marci, V. Augugliaro, L. Palmisano, E. Pramauro, Analytical control of photocatalytic treatments: degradation of a sulfonated azo dye, *J. Anal. Bioanal. Chem.* 378 (2004) 214–220.
- [12] S.C. Ameta, R. Chaudhary, R. Ameta, J. Vardia, A promising technology for wastewater treatment, *Indian Chem. Soc.* 80 (2003) 257–265.
- [13] D.A. Friesen, J.V. Headley, C.H. Langford, The photooxidative degradation of N-methylpyrrolidinone in the presence of $\text{CS}_3\text{PW}_{12}\text{O}_{40}$ and TiO_2 colloid photocatalysts, *J. Environ. Sci. Technol.* 33 (1999) 3193–3198.
- [14] L. Chen, J. He, Q. Yuan, Y. Liu, C.-T. Au, S.-F. Yin, Environmentally benign synthesis of branched $\text{Bi}_2\text{O}_3\text{-Bi}_2\text{S}_3$ photocatalysts by an etching and re-growth method, *J. Mater. Chem. A* 3 (2015) 1096–1102.
- [15] G. Manna, R. Bose, N. Pradhan, Photocatalytic $\text{Au-Bi}_2\text{S}_3$ hetero-nanostructures, *Angew. Chem. Int. Ed.* 53 (2014) 6743–6746.
- [16] G. Sagarzazu, K. Inoue, M. Saruyama, M. Sakamoto, T. Teranishi, S. Masuo, N. Tamai, Ultrafast dynamics and single particle spectroscopy of Au-CdSe nanorods, *Phys. Chem. Chem. Phys.* 15 (2013) 2141–2152.
- [17] E. Shaviv, O. Schubert, M. Alves-Santos, G. Goldoni, R. Di Felice, F. Valle, N. Del Fatti, U. Banin, C. Scnnichsen, Absorption properties of metal-semiconductor hybrid nanoparticles, *ACS Nano* 5 (2011) 4712–4719.
- [18] I. Majeed, M. Amtiaz Nadeem, M. Al-Oufi, M. Arif Nadeem, G.I.N. Waterhouse, A. Badshah, J.B. Metson, H. Idriss, On the role of metal particle size and surface coverage for photo-catalytic hydrogen production: a case study of the Au/CdS system, *Appl. Catal. B* 182 (2016) 266–276.
- [19] B.H. Wu, W.T. Liu, T.Y. Chen, T.P. Peng, J.H. Huang, L.J. Chen, Plasmon-enhanced photocatalytic hydrogen production on Au/TiO_2 hybrid nanocrystal arrays, *Nano Energy* 27 (2016) 412–419.
- [20] W.Y. Lei, T.T. Zhang, P. Liu, J.A. Rodriguez, G. Liu, M.H. Liu, Bandgap- and local field-dependent photoactivity of $\text{Ag/black phosphorus nanohybrids}$, *ACS Catal.* 6 (2016) 8009–8020.
- [21] D. Xu, D. Liu, T. Xie, Y. Cao, J.G. Wang, Z.J. Ning, Y.T. Long, H. Tian, Plasmon resonance scattering at perovskite $\text{CH}_3\text{NH}_3\text{PbI}_3$ coated single gold nanoparticles: evidence for electron transfer, *Chem. Commun.* 52 (2016) 9933–9936.
- [22] X. Liu, C. Lee, W.-C. Law, D. Zhu, M. Liu, M. Jeon, J. Kim, P.N. Prasad, C. Kim, M.T. Swihart, $\text{Au-Cu}_2\text{-xSe}$ heterodimer nanoparticles with broad localized surface plasmon resonance as contrast agents for deep tissue imaging, *Nano Lett.* 13 (2013) 4333–4339.
- [23] Amit Kumar Dutta, Swarup Kumar Maji, Kamala Mitra, Arpita Sarkar, Namrata Saha, Abhisek Brata Ghosh, Bibhutoosh Adhikary, Single source precursor approach to the synthesis of Bi_2S_3 nanoparticles: a new amperometric hydrogen peroxide biosensor, *J. Sens. Actuators B: Chem.* 192 (2014) 578–585.
- [24] B. Miller, A. Heller, Semiconductor liquid junction solar cells based on anodic sulphide films, *Nature* 262 (1976) 680–681.
- [25] R.N. Bhattacharya, P. Pramanik, Semiconductor liquid junction solar cell based on chemically deposited Bi_2S_3 thin film and some semiconducting properties of bismuth chalcogenide, *J. Electrochem. Soc.* 129 (1982) 332–335.
- [26] J.M. Ma, Z.F. Liu, J.B. Lian, X.C. Duan, T. Kim, P. Peng, X.D. Liu, Q. Chen, G. Yao, W.J. Zheng, Ionic liquids-assisted synthesis and electrochemical properties of Bi_2S_3 nanostructures, *CrystEngComm* 13 (2011) 3072–3079.
- [27] K. Yao, W.W. Gong, Y.F. Hu, X.L. Liang, Q. Chen, L.M. Peng, Individual Bi_2S_3 nanowire-based room-temperature H_2 sensor, *J. Phys. Chem. C* 112 (2008) 8721–8724.
- [28] H.F. Bao, C.M. Li, X.Q. Cui, Y. Gan, Q.L. Song, J. Guo, Synthesis of a highly ordered single-crystalline Bi_2S_3 nanowire array and its metal/semiconductor/metal back-to-back schottky diode, *Small* 4 (2008) 1125–1129.
- [29] K. Biswas, L.D. Zhao, M.G. Kanatzidis, Tellurium-Free thermoelectric the anisotropic n-type semiconductor Bi_2S_3 , *Adv. Energy Mater.* 2 (2012) 634.
- [30] B. Zhang, X.C. Ye, W.Y. Hou, Y. Zhao, Y. Xie, Biomolecule-assisted synthesis and electrochemical hydrogen storage of Bi_2S_3 flowerlike patterns with well-aligned nanorods, *J. Phys. Chem. B* 110 (18) (2006) 8978–8985.
- [31] R. Vogel, P. Hoyer, H.J. Weller, Quantum-sized PdS , CdS , AgS , Sb_2S_3 and Bi_2S_3 particles as sensitizers for various nanoporous wide bandgap semiconductors, *J. Phys. Chem.* 98 (1994) 3183–3188.
- [32] Y. Luo, H. Chen, X. Li, Z. Gong, X. Wang, X. Peng, M. He, Z. Sheng, Wet chemical synthesis of Bi_2S_3 nanorods for efficient photocatalysis, *J. Mater. Lett.* 105 (2013) 12–15.
- [33] H. Lim, J. Lee, S. Jin, J. Kim, J. Yoon, T. Hyeon, Highly active heterogeneous Fenton catalyst using iron oxide nanoparticles immobilized in alumina coated mesoporous silica, *J. Chem. Commun.* 4 (2006) 463–465.
- [34] C. Gonzalez-Arellano, J.M. Campelo, D.J. Macquarrie, J.M. Marinas, A.A. Romero, R. Luque, Efficient microwave oxidation of alcohols using low loaded supported metallic iron nanoparticles, *J. Chem. Sus. Chem.* 1 (2008) 746–750.
- [35] T. Zeng, W.W. Chen, C.M. Cirtiu, A. Moores, G. Song, C.J. Li, Fe_3O_4 nanoparticles: a robust and magnetically recoverable catalyst for three-component coupling of aldehyde, alkyne and amine, *J. Green Chem.* 12 (2010) 570–573.
- [36] T.S. Kim, J.K. Kim, K. Choi, M.K. Stenstrom, K.D. Zoh, Degradation mechanisms and the toxicity assessment in TiO_2 photocatalysis and photolysis of parathion, *J. Chemosphere* 62 (2006) 926–933.
- [37] F.E. Osterloh, Inorganic nanostructures for photoelectrochemical and photocatalytic water splitting, *Chem. Soc. Rev.* 42 (6) (2013) 2294–2320.
- [38] R. Franking, L.S. Li, M.A. Lukowski, F. Meng, Y.Z. Tan, R.J. Hamers, S. Jin, Facile post-growth doping of nanostructured hematite photoanodes for enhanced photoelectrochemical water oxidation, *Energy Environ. Sci.* 6 (2) (2013) 500–512.
- [39] A. Helal, F.A. Harraz, A.A. Ismail, T.M. Sami, I.A. Ibrahim, Controlled synthesis of bismuth sulfide nanorods by hydrothermal method and their photocatalytic activity, *Mater. Des.* 102 (2016) 202–212.
- [40] M. Grätzel, *Heterogeneous Photochemical Electron Transfer*, CRC Press, Baton Rouge, LA, 1988.
- [41] J. Tauc, R. Grigorovici, A. Vanuc, Optical properties and electronic structure of Ge, *Phys. Stat. Sol.* 15 (1966) 15627.
- [42] A.R.H.F. Ettema, C. Haas, An X-ray photoemission spectroscopy study of interlayer charge transfer in some misfit layer compounds, *J. Phys.: Condens. Matter* 5 (1993) 3817.
- [43] J. Grigas, E. Talik, V. Lazauskas, X-ray photoelectron spectra and electronic structure of Bi_2S_3 crystals, *Phys. Status Solidi B* 232 (2002) 220–230.
- [44] Z. Xu, M. Zhang, J. Wu, J. Liang, L. Zhou, B. Lu, Visible light-degradation of azo dye methyl orange using $\text{TiO}_2/\beta\text{-FeOOH}$ as a heterogeneous photo-Fenton-like catalyst, *Water Sci. Technol.* 68 (2013) 2178–2185.
- [45] F.A. Harraz, Synthesis and surface properties of magnetite (Fe_3O_4) nanoparticles infiltrated into porous silicon template, *Appl. Sur. Sci.* 287 (2013) 203–210.
- [46] T. Yamashita, P. Hayes, Analysis of XPS spectra of Fe^{2+} and Fe^{3+} ions in oxide materials, *Appl. Sur. Sci.* 254 (2008) 2441–2449.
- [47] H. Bao, C.M. Li, X. Cui, Q. Song, H. Yang, J. Guo, Single-crystalline Bi_2S_3 nanowire network film and its optical properties, *Nanotechnology* 19 (33) (2008), Article ID 335302.

- [48] H. Wang, X. Zhang, B. Liu, H. Zhao, Y. Li, Y. Huang, Z. Du, Synthesis and characterization of single crystal α - Fe_2O_3 nanobelts, *Chem. Lett.* 34 (2005) 184–185.
- [49] F.A. Harraz, A.A. Ismail, S.A. Al-Sayari, A. Al-Hajry, Novel α - Fe_2O_3 /polypyrrole nanocomposite with enhanced photocatalytic performance, *J. Photochem. Photobiol. A: Chem.* 299 (2015) 18–24.
- [50] Q. Zhang, L. Gao, J. Guo, Effects of calcination on the photocatalytic properties of nanosized TiO_2 powders prepared by TiCl_4 hydrolysis, *Appl. Catal. B: Environ.* 26 (2000) 207–215.
- [51] Y. Peng, K.K. Wang, T. Liu, J. Xu, B.G. Xu, Synthesis of one-dimensional Bi_2O_3 - $\text{Bi}_2\text{O}_{2.33}$ heterojunctions with high interface quality for enhanced visible light photocatalysis in degradation of high-concentration phenol and MO dyes, *Appl. Catal. B: Environ.* 203 (2017) 946–954.
- [52] X. Liu, N. Chen, Y. Li, D. Deng, X. Xing, Y. Wang, A general nonaqueous sol-gel route to g- C_3N_4 -coupling photocatalysts: the case of Z-scheme g- C_3N_4 / TiO_2 with enhanced photodegradation toward RhB under visible-light, *Sci. Rep.* 6 (2016) 39531.
- [53] P. Cai, S.-M. Zhou, D.-K. Ma, S.-N. Liu, W. Chen, S.-M. Huang, Fe_2O_3 -modified porous BiVO_4 nanoplates with enhanced photocatalytic activity, *Nano-Micro Lett.* 7 (2) (2015) 183–193, <http://dx.doi.org/10.1007/s40820-015-0033-9>.
- [54] N. Liang, J.T. Zai, M. Xu, Q. Zhu, X. Wei, X.F. Qian, Novel $\text{Bi}_2\text{S}_3/\text{Bi}_2\text{O}_2\text{CO}_3$ heterojunction photocatalysts with enhanced visible light responsive activity and wastewater treatment, *J. Mater. Chem. A* 2 (2014) 4208–4216.
- [55] N. Liang, M. Wang, L. Jin, S.S. Huang, W.L. Chen, MXuQQ, He, J.T. Zai, N.H. Fang, X.F. Qian, Highly efficient $\text{Ag}_2\text{O}/\text{Bi}_2\text{O}_2\text{-CO}_3$ p-n heterojunction photocatalysts with improved visible light responsive activity, *ACS Appl. Mater. Interfaces* 6 (14) (2014) 11698–11705.
- [56] H.F. Cheng, B.B. Huang, X.Y. Qin, X.Y. Zhang, Y. Dai, A controlled anion exchange strategy to synthesize Bi_2S_3 nanocrystals/ BiOCl hybrid architectures with efficient visible light photoactivity, *Chem. Commun.* 48 (2012) 97–99.
- [57] P. Madhusudan, J.R. Ran, J. Zhang, J.G. Yu, G. Liu, Novel urea assisted hydrothermal synthesis of hierarchical $\text{BiVO}_4/\text{Bi}_2\text{O}_2\text{CO}_3$ nanocomposites with enhanced visible-light photocatalytic activity, *Appl. Catal. B* 110 (2011) 286–295.
- [58] G.K. Pradhan, D.K. Padhi, K.M. Parida, Fabrication of α - Fe_2O_3 nanorod/RGO composite: a novel hybrid photocatalyst for phenol degradation, *ACS Appl. Mater. Interfaces* 5 (18) (2013) 9101–9110.
- [59] Y. Shi, H.Y. Li, L. Wang, W. Shen, H.Z. Chen, Novel α - Fe_2O_3 /CdS cornlike nanorods with enhanced photocatalytic performance, *ACS Appl. Mater. Interfaces* 4 (9) (2012) 4800–4806.
- [60] J. Lv, T. Kako, Z. Zou, J. Ye, Band structure design and photocatalytic activity of $\text{In}_2\text{O}_3/\text{N-InNbO}_4$ composite, *Appl. Phys. Lett.* 95 (2009), 032107.
- [61] H. He, S.P. Berglund, P. Xiao, W.D. Chemelewski, Y. Zhang, C.B. Mullins, Nanostructured $\text{Bi}_2\text{S}_3/\text{WO}_3$ heterojunction films exhibiting enhanced photoelectrochemical performance, *J. Mater. Chem. A* 1 (2013) 12826–12834.
- [62] Y. Xu, M.A.A. Schoonen, The absolute energy positions of conduction and valence bands of selected semiconducting minerals, *Am. Mineral.* 85 (2000) 543–556.
- [63] E. Pineda, M.E. Nicho, P.K. Nair, H. Hu, Optoelectronic properties of chemically deposited Bi_2S_3 thin films and the photovoltaic performance of $\text{Bi}_2\text{S}_3/\text{P3OT}$ solar cells, *Sol. Energy* 86 (2012) 1017–1022.
- [64] Y.-Q. Zhang, S. Li, B.-P. Zhang, Controllable synthesis of $\text{Bi}_2\text{S}_3/\text{CuS}$ heterostructures by an in situ ion-exchange solvothermal process and their enhanced photocatalytic performance, *RSC Adv.* 6 (2016) 103215–103223.
- [65] H.B. Fu, C.S. Pan, W.Q. Yao, Y.F. Zhu, Visible-light-induced degradation of rhodamine B by nanosized Bi_2WO_6 , *J. Phys. Chem. B* 109 (2005) 22432–22439.